



# Role of Powder Treatment and Carbon Nanotube Dispersion in the Fracture Toughening of Plasma-Sprayed Aluminum Oxide—Carbon Nanotube Nanocomposite

Kantesh Balani, Srinivasa Rao Bakshi, Yao Chen, Tapas Laha, and Arvind Agarwal\*

*Mechanical and Materials Engineering Department, EAS 3464, Miami, FL-33174, USA*

Al<sub>2</sub>O<sub>3</sub> ceramic reinforced with 4-wt% multiwalled carbon nanotube (CNT) is plasma sprayed for improving the fracture toughness of the nanocomposite coating. Two different methodologies of CNT addition have been adopted in the powder feedstock to assist CNT dispersion in the nano-Al<sub>2</sub>O<sub>3</sub> matrix. First, spray-dried nano-Al<sub>2</sub>O<sub>3</sub> agglomerates are *blended* with 4 wt% CNT as powder-feedstock, which is subsequently plasma sprayed resulting in the fracture toughness improvement of 19.9%. Secondly, spray dried *composite* nano-Al<sub>2</sub>O<sub>3</sub> and 4 wt% CNT powder was used as feedstock for attaining improved dispersion of CNTs. Plasma sprayed coating of composite spray dried powder resulted in increase of 42.9% in the fracture toughness. Coating synthesized from the blended powder displayed impact alignment of CNTs along splat interface, and CNTs chain loop structure anchoring the fused Al<sub>2</sub>O<sub>3</sub> melt whereas coating synthesized from composite spray dried powder evinced anchoring of CNTs in the solid state sintered region and CNT mesh formation. Enhanced fracture toughness is attributed to significance of CNT dispersion.

**Keywords:** Carbon Nanotubes, Nanocomposites, Toughness.

## 1. INTRODUCTION

Al<sub>2</sub>O<sub>3</sub> (aluminum oxide) ceramic is used for wear and impact resistant coatings, line inserts, heat exchangers, etc., due to its excellent compression strength, high hardness and wear resistance at high temperatures.<sup>1–5</sup> However, the applications of Al<sub>2</sub>O<sub>3</sub> are limited due to its brittle behavior.<sup>2–5</sup> Due to their excellent mechanical properties, carbon nanotubes (CNTs) have been used as reinforcing material, largely for polymeric matrices. A very few researchers have added CNTs to ceramic matrices such as SiC, TiO<sub>2</sub>, Si<sub>3</sub>N<sub>4</sub>, hydroxyapatite and Al<sub>2</sub>O<sub>3</sub>, for improvement of fracture toughness.<sup>6–14</sup> CNT additions in Al<sub>2</sub>O<sub>3</sub> matrix has shown bending strength improvement of upto 10%.<sup>15</sup> Zhan et al. have shown three times improvement in the fracture toughness of spark plasma sintered CNT-alumina composite compared to that of pure alumina.<sup>12, 16–22</sup> On the contrary, Wan et al claimed that CNT-alumina did not possess high fracture toughness but improved contact-damage resistance.<sup>13</sup> The discrepancy in the fracture toughness data of the two studies could be attributed to the use of different indentation techniques by the two research groups. Hence

the absence of a widely accepted fracture toughening mechanism in CNT-ceramic nanocomposite has kept researchers in contradiction. Although it has been observed that fracture toughness is governed by CNT pullout, crack deflection and crack bridging,<sup>23, 24</sup> the fundamental reason of attaining the enhanced fracture toughness and its relation to nanotube dispersion still remains unclear.<sup>23</sup>

Importance of CNT as a dispersed phase is already impressed upon by various research works, with dispersion being achieved by sol–gel technique, surface activation, inorganic coating, heterocoagulation, ball milling, solvent incorporation, etc.<sup>25–32</sup> Dispersed CNTs allow interfacial interactions and load-transfers towards attaining improved mechanical properties in ceramic nanocomposites. However, strong agglomeration tendency of CNTs poses the challenge of uniform dispersion.

In the current work, plasma spraying technique has been adopted to synthesize Al<sub>2</sub>O<sub>3</sub>-CNT nanocomposite coating using two different kind of powder feedstock to obtain improved dispersion of CNTs. Idea of utilizing two strategies is to understand the fracture toughening enhancement of the plasma sprayed coatings as a function of CNT dispersion. Uniform dispersion of CNTs in large scale coatings and bulk structures remains a challenge for researchers.<sup>33–37</sup> Our

\*Author to whom correspondence should be addressed.

research group is the first one to demonstrate that multiwalled carbon nanotubes can be successfully plasma sprayed and can survive the harsh environment of temperature and impact in metal (Al) matrix-CNT nanocomposite.<sup>38–40</sup>

## 2. EXPERIMENTAL DETAILS

### 2.1. Powder Treatment

Nanosize powders cannot be plasma sprayed owing to its tendency of clogging the plasma gun nozzle.<sup>41</sup> High surface friction among fine powder particles leads to inconsistent flow producing non-homogeneous, and inferior coatings.<sup>40</sup> Hence, powder treatment becomes a necessity in exercising them as required feedstock. Two powder treatments were adopted in realizing the dispersion of CNTs in the nano- $\text{Al}_2\text{O}_3$  matrix. First treatment involved spray drying of nano- $\text{Al}_2\text{O}_3$  powders followed by blending with CNTs in a jar mill. Second powder treatment utilized spray drying of slurry of nano- $\text{Al}_2\text{O}_3$  particles and CNT to result in composite spherical agglomerates. Resulting spherical agglomerates (in 15–60  $\mu\text{m}$  size range ideal for plasma spraying) cause reduced interparticle friction and avoid clogging of powders in the nozzle. Details of the powder treatment are as follows:

#### 2.1.1. Blending of Spray Dried Nano- $\text{Al}_2\text{O}_3$ with 4 wt% CNT (AC-B)

Spray drying is a process where nanosize powder particles are dispersed in an aqueous organic binder to form slurry. The slurry is passed through an atomizing orifice,

which mechanically binds the fine particles as spherical agglomerates. Spray drying was carried out at a commercial vendor's facility. Spray drying of nano- $\text{Al}_2\text{O}_3$  (referred to as A-SD) powders results in spherical agglomerates (15–60  $\mu\text{m}$  in diameter) as shown in Figure 1(b). A-SD powder was blended with 4 wt% CNTs (95%+ purity, OD 40–70 nm, 0.5–2.0  $\mu\text{m}$  in length) in a jar mill to result the powder feedstock (referred to as AC-B powder). In AC-B powder, nanotubes disperse onto (i) surface of spray dried agglomerate and (ii) dome-cavity of spray dried powder. Morphology of as-received nano- $\text{Al}_2\text{O}_3$ , A-SD powder and resulting AC-B powder has been schematically shown along with the SEM images in Figure 1.

#### 2.1.2. Composite Spray Drying of Nano- $\text{Al}_2\text{O}_3$ and 4 wt% CNT (AC-SD)

Spray drying of composite nano- $\text{Al}_2\text{O}_3$  powder and 4 wt% CNTs (referred to as AC-SD) produced spherical agglomerates of 15–60  $\mu\text{m}$ , Figure 2(a). No agglomeration of CNTs was observed along the powder surface, Figure 2(b), and CNTs were distributed uniformly inside the powder agglomerate, as seen in the fractured powder surface Figure 2(c). Spray drying resulted in improved dispersion of CNTs as compared to blended powder (AC-B). Details of initial particle size, spray drying treatment, and adopted nomenclature is presented in Table I.

### 2.2. Plasma Spraying and Characterization

Plasma spraying was carried out using Praxair SG 100 gun on an AISI 1020 steel substrate. In-flight particle diagnostic sensor AccuraSpray (Tecnar Automation Ltée,

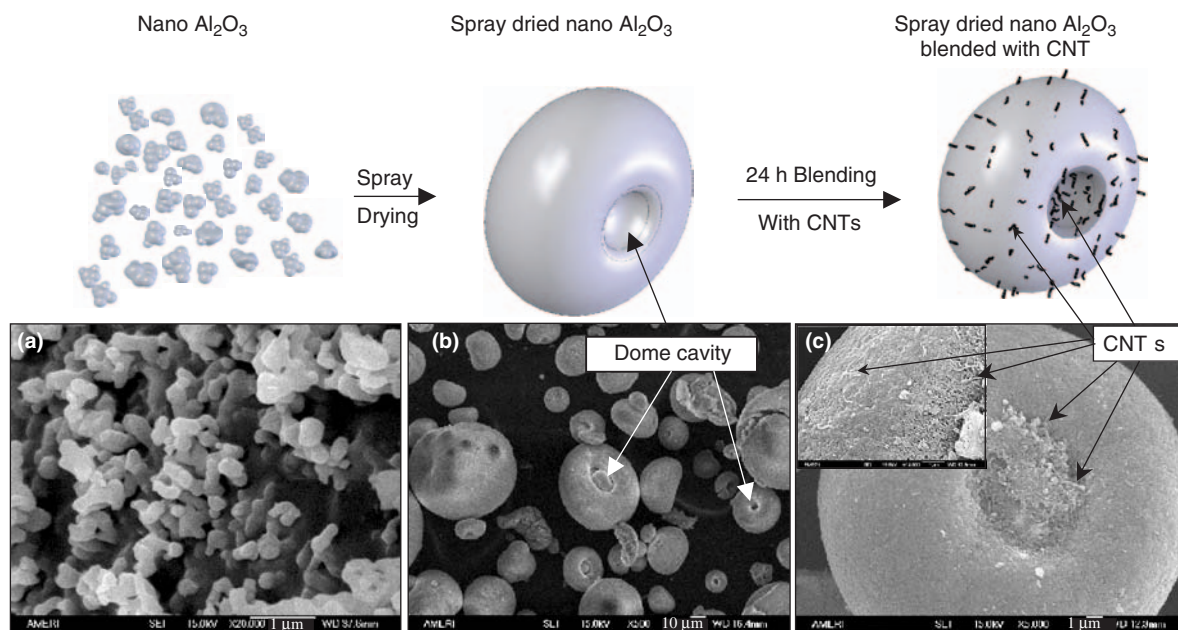


**Fig. 1.** Process schematic and SEM images of (a) nano  $\text{Al}_2\text{O}_3$ , (b) Spray dried nano- $\text{Al}_2\text{O}_3$  (A-SD) agglomerates, and (c) spray dried nano- $\text{Al}_2\text{O}_3$  blended with 4 wt% CNT for 24 h to result nanocomposite AC-B powder feedstock.

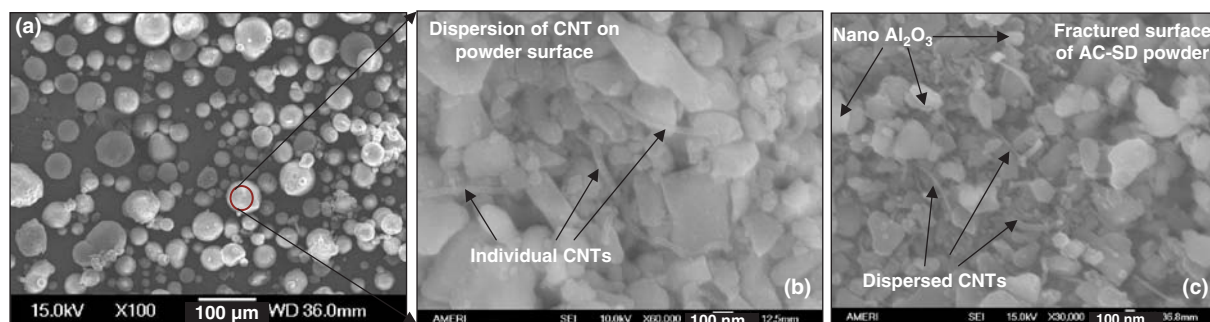


**Fig. 2.** SEM image of AC-SD powder showing (a) powder agglomerates, (b) dispersion of CNTs as separate entities on surface, and (c) fractured surface showing inside of the powder.

QC, Canada) was used to measure particle velocity and temperature during plasma spraying. Representative plasma-processing parameters are listed in Table II. Field emission-scanning electron microscope JEOL JSM 6330 F was used for investigating microstructural features. Micro Raman spectroscopy was performed using Ar laser at a wavelength of 514 nm. XRD spectrum was obtained using Siemens D-500 operating at 40 kV and 20 mA with  $\text{CuK}\alpha$  peak of 1.54 Å. Image-Pro® Plus, Version 5.1 imaging software (2004 Media Cybernetics Inc.) has been utilized for quantitative image analysis. Shanghai Taiming Optical Instruments, Zhongguo, HXD-100 TMC microhardness tester (200 g load and 15 s dwell time) was used for estimating hardness and fracture toughness of the plasma sprayed samples using Vicker's indentation technique. Student t-test was utilized, with better than 95% confidence level, towards comparing the statistical difference between the fracture toughness values for eight indentations on each sample. Philips PW 6061 TEM system (CM 200, Eindhoven, Netherlands) was utilized for transmission electron microscopy.

### 3. RESULTS AND DISCUSSION

#### 3.1. CNT Dispersion in Spray Dried $\text{Al}_2\text{O}_3$ (AC-B) Powder

Nano scale surfaces are known to be unstable because of their high surface to volume ratio, and have strong tendency

towards agglomeration.<sup>42</sup> During mechanical blending of the powder mixture, agglomeration and settling of CNTs in the dome cavity is observed in the scattergram, Figure 3(a), via Image Pro quantitative analysis. Agglomeration of CNTs in the histogram, Figure 3(b), endorses the higher CNT content in the dome cavity when compared to the CNTs adhering at the surface of the powder agglomerate. Though CNTs are dispersed in AC-B powder to some extent, further improvisation of CNT dispersion can have tremendous impact on improving mechanical properties of the nanocomposite. This is achieved by composite spray drying of the powder as explained in the following section.

#### 3.2. CNT Dispersion in Spray Dried (AC-SD) Powder

Laplace equation (of free energy change with particle radius) clearly elicits the instability of nanoparticles with the decreasing radius of particles. But, increasing the surface area by contacting two unstable surfaces reduces the overall energy of system to a lower value. CNTs, when mixed with nano- $\text{Al}_2\text{O}_3$  powder particles (during composite spray drying), reduce the surface charges by physically attaching to open surfaces.<sup>43</sup> Because of high surface area of nano- $\text{Al}_2\text{O}_3$  particles, CNTs do not find difference in associating itself with nano- $\text{Al}_2\text{O}_3$ .<sup>43</sup> Surface energy of CNTs range about  $0.2 \text{ J/m}^2$ , whereas  $\text{Al}_2\text{O}_3$  particles have surface energy of  $\sim 1.59 \text{ J/m}^2$ .<sup>244</sup> It has been shown that Al-graphite interface can bring down the energy in the  $0.02\text{--}0.4 \text{ J/m}^2$  range.<sup>44</sup> Nano- $\text{Al}_2\text{O}_3$  powder particles

**Table I.** Initial powder size, spray drying treatment and adopted nomenclature.

Initial powders	Powder treatment (Step 1)	Powder treatment	Resulting powder (Step 2)	CNT dispersion	Plasma Sprayed coating nomenclature
$\text{Al}_2\text{O}_3$ (150 nm particle size)	Spray drying of $\text{Al}_2\text{O}_3$ (agglomerate $\sim 15\text{--}60 \mu\text{m}$ )	—	A-SD ( $\text{Al}_2\text{O}_3$ agglomerate $\sim 15\text{--}60 \mu\text{m}$ )	—	A-SD Coating ( $\text{Al}_2\text{O}_3$ )
CNTs (Multi walled, OD 40–70 nm, 0.5–2.0 $\mu\text{m}$ long)	Spray drying of $\text{Al}_2\text{O}_3$ (agglomerate $\sim 15\text{--}60 \mu\text{m}$ )	Blending with 4 wt% CNTs for 24 h	AC-B ( $\text{Al}_2\text{O}_3\text{--}4 \text{ wt}\%$ CNT agglomerate $\sim 15\text{--}60 \mu\text{m}$ )	Onto surface and dome cavity	AC-B Coating ( $\text{Al}_2\text{O}_3\text{--}4 \text{ wt}\%$ CNT)
	Spray drying of $\text{Al}_2\text{O}_3$ and 4 wt% CNTs (agglomerate $\sim 15\text{--}60 \mu\text{m}$ )	—	AC-SD ( $\text{Al}_2\text{O}_3\text{--}4 \text{ wt}\%$ CNT agglomerate $\sim 15\text{--}60 \mu\text{m}$ )	Throughout the powder agglomerate	AC-SD Coating ( $\text{Al}_2\text{O}_3\text{--}4 \text{ wt}\%$ CNT)

**Table II.** Representative plasma spray processing parameters.

Plasma parameters	Volts (V)	Current (Amp)	Primary gas (slm)	Secondary gas (slm)	Carrier gas (slm)	Power (kW)
Sprayed Coatings	35–40	650–800	Ar (32.1)	He (59.5)	Ar (19.8)	25–30

thereby aid dispersion of CNTs in the solid state mixing of nanocomposite powder.<sup>45</sup> Random surface availability therefore results in the uniform dispersion of CNTs. Distribution of CNTs in the AC-SD powder feedstock as a function of their aspect ratio is presented in Figure 4. Figure 4 shows non-preferential distribution of CNTs throughout the powder agglomerate. Visually no bundles/agglomerates of CNTs were observed in the spray dried powder endorsing the non-preferred sticking sites for CNTs. Fractured AC-SD powder was analyzed for observing excellent CNT dispersion in the core of spray dried agglomerate. Aspect ratio is helpful in understanding the pinning effect of CNTs, and corresponding dispersion angle suffices the reinforcement in the subsequent direction.

### 3.3. Coating Structure and Morphology

Figures 5(a) and (b) show plasma sprayed AC-B and AC-SD nanocomposite coating respectively on the AISI 1020 steel substrate. Uniform and homogeneous AC-B and AC-SD nanocomposite coatings about 350–400  $\mu\text{m}$  thick

are obtained. The coatings are free from cracks and adherent to the substrate. Figures 5(a) and (b) show *two* distinct regions of *partially-melted/solid-state sintered* regions and *fully melted* regions in nanocomposite coating. This bimodal structure in the coating is attributed to 30–45% porosity in spray dried powder agglomerate<sup>46</sup> coupled with controlled plasma parameters. Owing to poor thermal conductivity of porous spray dried agglomerate, partial melting is sustained in the core whereas fully melted region is obtained on the surface. The surface melting of powder particles results fully melted and re-solidified regions whereas the core of the powder agglomerate gets sintered in solid state. Image analysis of coatings and Table III evinced higher percentage (~82.4%) of fully melted and re-solidified region in AC-B coating when compared to that of AC-SD coating (71.4%). Higher degree of melting in AC-B coating is also attributed to the dispersion behavior and thermal conductivity of CNTs. Thermal conductivity of CNTs<sup>14</sup> ( $\sim 3 \times 10^3 \text{ W/m} \cdot \text{K}$ ) is significantly higher than

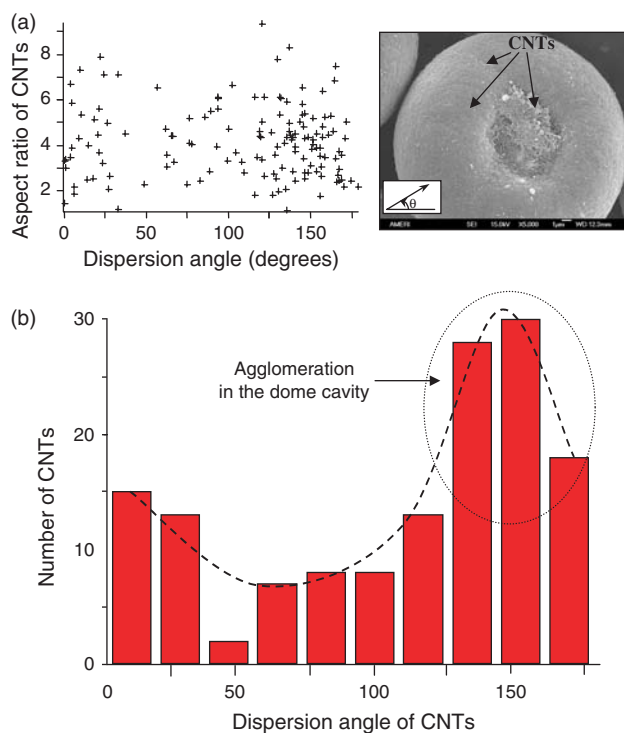


**Fig. 3.** (a) Scattergram and representative micrograph describing CNT dispersion angle with respect to aspect ratio, and (b) Histogram of AC-B powder depicting agglomeration of CNTs in the dome cavity of the powder agglomerate.

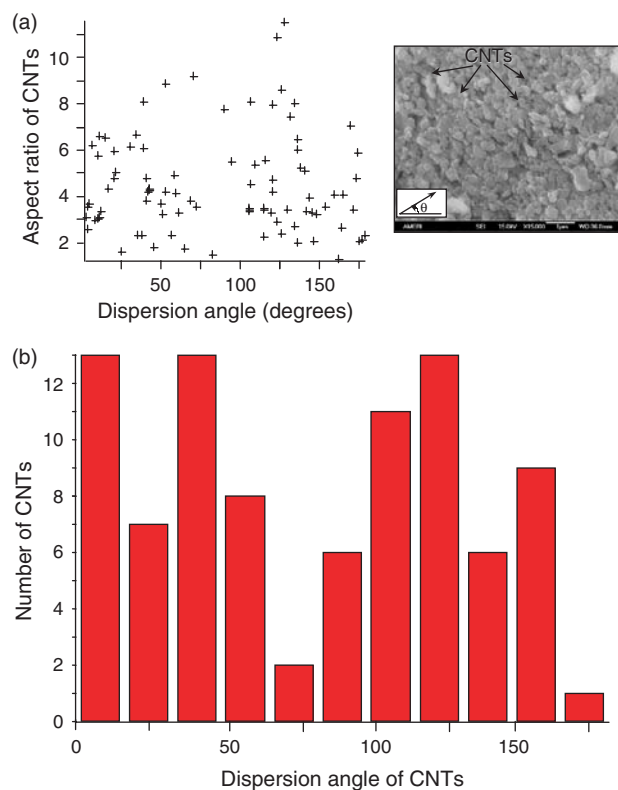


**Fig. 4.** (a) Scattergram and representative micrograph describing CNT dispersion angle with respect to aspect ratio, and (b) Histogram of AC-SD powder depicting dispersion angle with respect to the number of CNTs in the powder agglomerate.

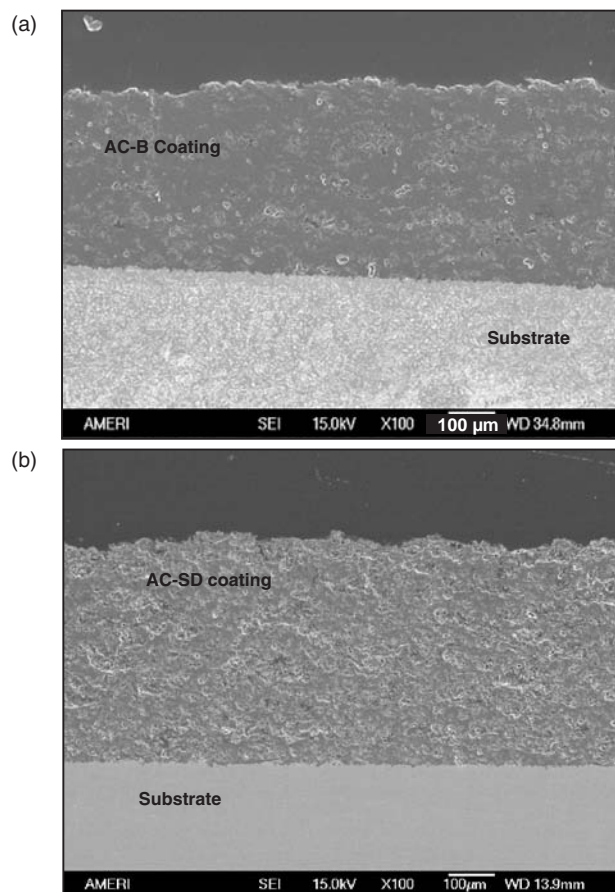


**Fig. 5.** Plasma sprayed (a) AC-B coating and (b) AC-SD nanocomposite coating (thickness  $\sim 350 \mu\text{m}$ ) on a steel substrate.

$\text{Al}_2\text{O}_3$  ( $\sim 5.90$  to  $36.16 \text{ W/m.K}$ ).<sup>47</sup> During plasma spraying, AC-B powder agglomerate gets superheated due to higher density of CNTs on surface and in dome cavity resulting in high fraction of fully molten and re-solidified structure in the coating. High surface temperature of AC-B powder during plasma spraying was experimentally verified using in-flight particle diagnostic sensor. Though similar plasma processing parameters were used to deposit coating, AC-B powder experienced a temperature of  $2898 \text{ K}$  whereas AC-SD powder had a reduced temperature  $2332 \text{ K}$ . Corresponding mean velocities of  $271$  and  $244 \text{ m/s}$  were observed for AC-B and AC-SD powders respectively.

### 3.4. Carbon Nanotube Retention and Dispersion in Coating

During plasma spraying, the high velocity impact of spray particles in conjunction with heating/melting of agglomerates may result in re-distribution of CNTs in the microstructure. As observed from the Raman spectrum, Figure 6, D- and G-peaks are seen for CNTs in the plasma sprayed AC-B and AC-SD coatings. The ratio of G/D peak is higher indicating the retention of undamaged graphene structure in CNT. Since AC-B and AC-SD powders showed

**Table III.** Volume percentage of microstructural features of the plasma sprayed coatings obtained from quantitative microscopy and image analysis.

Coating	Fully melted	Partially melted	Porosity
$\text{nAl}_2\text{O}_3$ coating	80.91	15.85	3.24
AC-B coating	82.10	12.10	5.80
AC-SD coating	71.39	24.70	3.91

similar Raman peaks for CNTs, only one data is represented for powder feedstock in Figure 6. In-flight diagnostic sensor was also used to measure the velocity of AC-B and AC-SD powder particles in the plasma stream. The flight time of AC-B and AC-SD powders in the plasma plume was estimated as to  $3.7 \times 10^{-4} \text{ s}$  and  $4.1 \times 10^{-4} \text{ s}$  respectively. Hence rapid kinetics of plasma spraying is attributed to retaining undamaged CNTs in the plasma sprayed coatings. In addition, possible damage of CNTs from the harsh plasma environment is cloaked by poor thermal conductivity of porous spray dried agglomerates.

#### 3.4.1. Carbon Nanotubes in Plasma Sprayed AC-B Coating

As seen in Figure 7(a) interlinked and undamaged CNTs are retained in the plasma sprayed AC-B coating. CNT chain-loop formation acts as splat anchors. In addition, entangling of CNTs induce torsion, making torsion stiffness an important factor in providing toughness to the reinforced nanocomposite.<sup>48</sup> Successive impact of splats upon deposition has shown alignment of CNTs along splat interface in Figure 7(b). Alignment of CNTs at the interface of partially melted and fully melted region results in joining the two regions together. Some CNTs display diameter of  $100\text{--}125 \text{ nm}$  as compared to the starting diameter

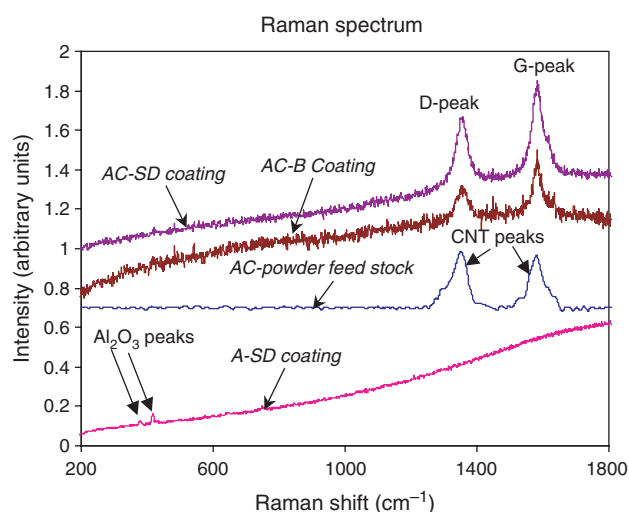


**Fig. 6.** Raman spectrum of plasma sprayed A-SD coating, initial powder feedstock, and plasma sprayed AC-B and AC-SD nanocomposite coatings. AC-Powder feedstock Raman spectrum is representative for AC-B and AC-SD powder feedstock.



Fig. 7. SEM image of AC-B coating depicting (a) fusion of CNTs in  $\text{Al}_2\text{O}_3$ , and (b) alignment of CNTs along splat interface.

of 40–70 nm. Increase in the nanotube diameter, and surface smoothness suggests that CNTs get coated with  $\text{Al}_2\text{O}_3$  during plasma spraying. Surface coating of  $\text{Al}_2\text{O}_3$  on CNT also shrouds it from the thermal damage during plasma spraying. Good wettability of CNTs is evident from the surface fusion of CNTs with the  $\text{Al}_2\text{O}_3$  matrix (Fig. 7(a)). On one hand, entrapped CNTs between splats (Fig. 7(b)) improve bending<sup>49</sup> and compressive toughness, the looping and fusion of CNTs (Fig. 7(a)) insinuates improvement in torsion stiffness<sup>48</sup> and toughness of the nanocomposite coating.

#### 3.4.2. Carbon Nanotubes in Plasma Sprayed AC-SD Coating

The cross-sectional image of AC-SD coating, Figure 8, presents the retention of CNT network as anchors, both in the fully melted and partially melted/solid state sintered regions. CNTs distributed in the core of the AC-SD powder get entrapped in the solid state sintered region, Figure 8(a). On the other hand, CNTs present on the surface of AC-SD powder get entrapped as bridge between two splats in the re-solidified region, Figure 8(b). Nano- $\text{Al}_2\text{O}_3$  particles attached closely with CNT surface in the powder feedstock

melts to form a thin coating over CNT during plasma spraying. Rapid solidification tends to freeze molten  $\text{Al}_2\text{O}_3$  layer suggesting excellent wettability between  $\text{Al}_2\text{O}_3$  with CNT. Rapid kinetics, therefore, might be reasoned to attribute enhanced wettability observed in the current work. Nucleation frequency ( $I_v$ ) of  $\text{Al}_2\text{O}_3$  on CNT surface at a temperature ( $T$ ) can be expressed by Eq. (1) as:<sup>50</sup>

$$I_v = K_v \exp\left(-\frac{\Delta G^* f(\theta)}{kT}\right) \quad (1)$$

where  $K_v$  is kinetic parameter,  $\theta$  is the wetting angle, and  $\Delta G^*$  is the excess free energy of the critical nucleus, and  $k$  is the Boltzmann constant. Since rapid solidification offers enhanced excess free energy for nucleation, it must be balanced by reduction in the wetting factor  $f(\theta)$ . The wetting factor expression<sup>51</sup>  $\{f(\theta) = (2 + \cos\theta)(1 - \cos\theta)^2/4\}$  further clarifies reduction of wetting angle (and enhanced wettability). Moreover, heterogeneous nucleation reduces the excess energy barrier of nucleation,<sup>51</sup> allowing rapid solidification of  $\text{Al}_2\text{O}_3$  by wetting CNT surface.

CNT is observed as the bridge between splats to prevent their separation as depicted in Figure 8(b). Thickening

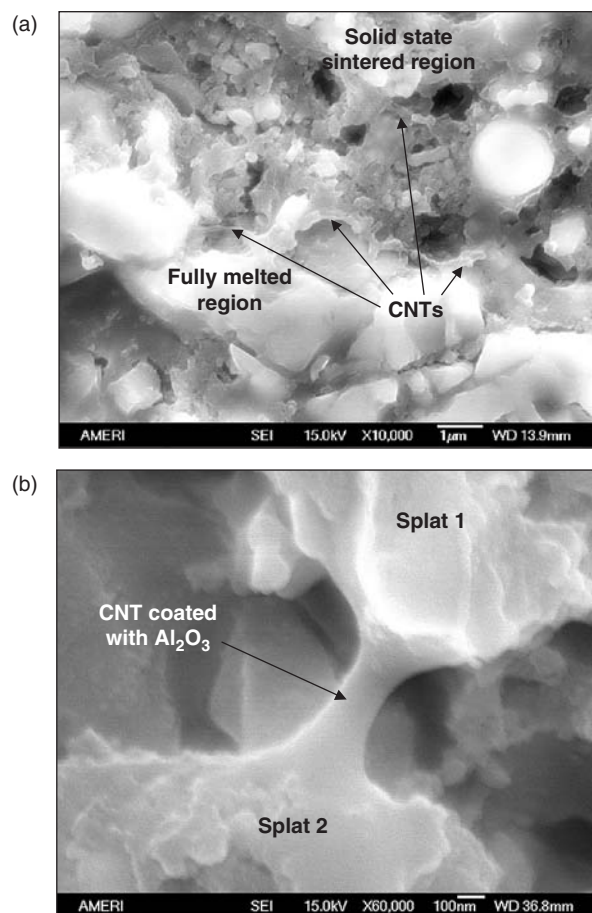
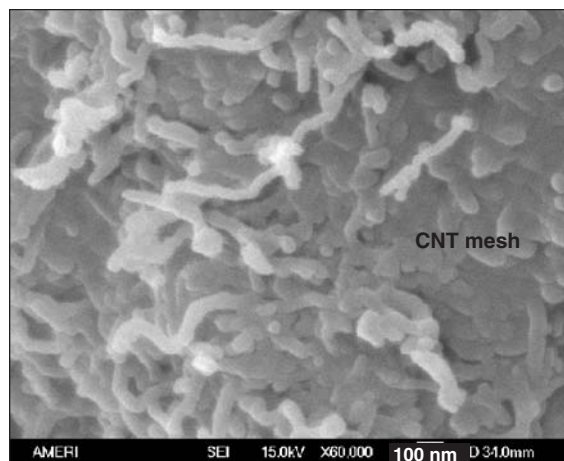
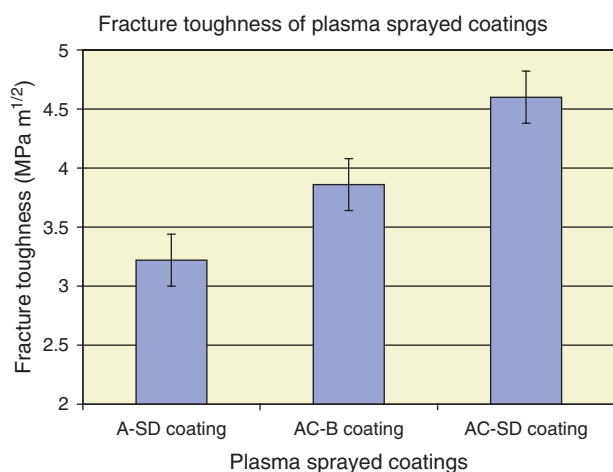


Fig. 8. Cross-sectional image of AC-SD coating showing dispersion of CNTs as (a) entrapped in the solid state sintered region, and (b) bridge anchoring between splats.



**Fig. 9.** SEM image of AC-SD coating illustrating CNT mesh formation by capillary action.

of CNT is caused by the flow of molten  $\text{Al}_2\text{O}_3$  over CNT surface. Curvature effect at the ends of CNT is due to the capillary action responsible for covering the CNT along its surface (Fig. 8(b)). Though we have observed increased wetting of CNT with molten  $\text{Al}_2\text{O}_3$ , currently there is no data on the determination of wetting angle<sup>52</sup> and interaction of  $\text{Al}_2\text{O}_3$  and CNTs. Figure 9 shows an interesting phenomenon of CNT mesh formation in AC-SD coating which can be explained in terms of wetting kinetics. Surface tension holds the molten  $\text{Al}_2\text{O}_3$  over CNT surface as a coating during plasma spraying. Since increased contact area leads to reduced surface energy,  $\text{Al}_2\text{O}_3$  coated CNTs come closer to each other. As the volume of molten  $\text{Al}_2\text{O}_3$  over CNTs increases, surface tension is not large enough to hold the molten liquid in place. Now capillarity has enough time to allow seeping down of molten surfaces to leave behind a meshed network of CNTs, Figure 9.<sup>53,54</sup> These phenomena require further understanding of surface tension and



**Fig. 10.** Fracture toughness of plasma sprayed coatings showing improvement of fracture toughness in CNT reinforced AC-B and AC-SD nanocomposite coatings.

capillarity equations in modeling the CNT- $\text{Al}_2\text{O}_3$  interface, which is our ongoing work.

### 3.5. Mechanical Property Evaluation

Microhardness of the plasma sprayed  $\text{Al}_2\text{O}_3$  was  $714.2 \pm 14.9 V_H$ , whereas plasma sprayed AC-B coating and AC-SD coating depicted hardness of  $709.6 \pm 8.4 V_H$  and  $738.7 \pm 12.9 V_H$  respectively. These measurements convey that there is no significant variation in the hardness

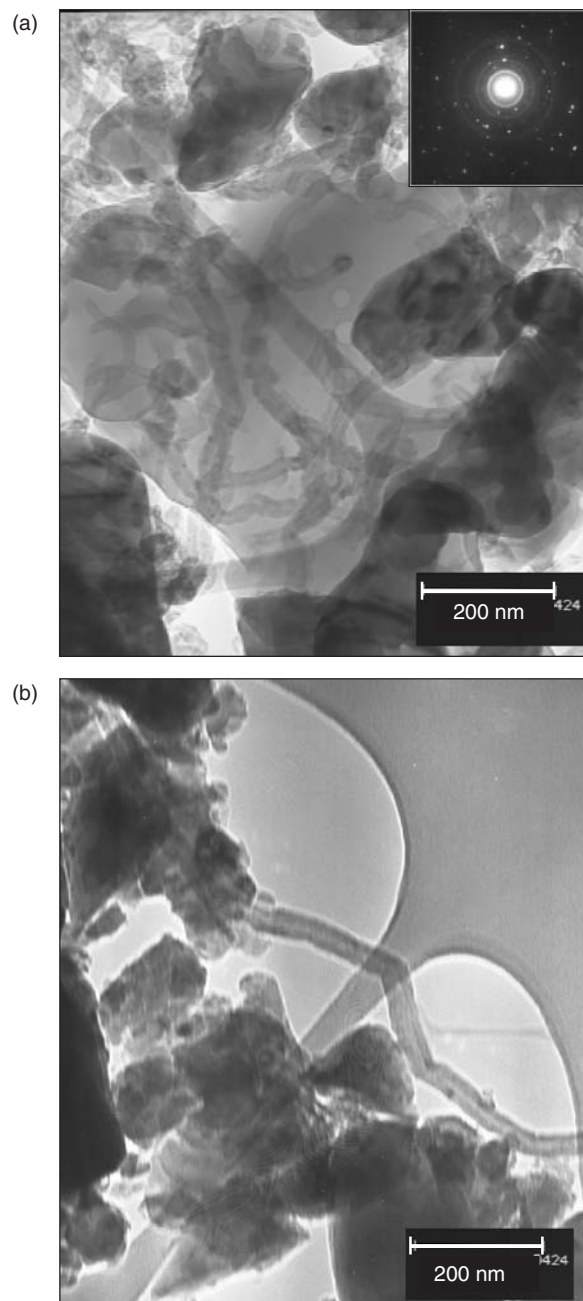


**Fig. 11.** TEM image showing (a) CNT agglomeration and dispersed nano- $\text{Al}_2\text{O}_3$  particles in AC-B coating, and (b) dispersed CNT anchoring in  $\text{Al}_2\text{O}_3$  is depicted in AC-SD coating.

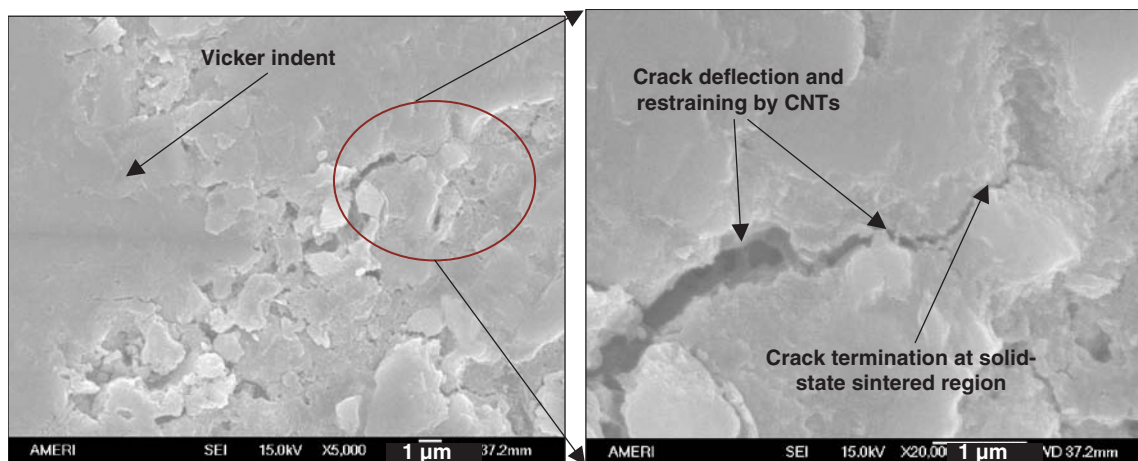


Fig. 12. Vicker indentation crack in AC-SD coating is being resisted by CNT bridges and crack-termination at solid-state sintered region.

value of the plasma sprayed coatings. Higher percentage of re-solidified structure in AC-B coating tends to increase the hardness in comparison to AC-SD coating, whereas poor dispersion of CNT (when compared to AC-SD coating) balances the lowering of hardness. Improved dispersion of CNTs in the AC-SD coating is also corroborated later in the transmission electron microscopy (TEM) analysis in Figure 11.

Fracture toughness of both coatings was calculated from the Antis semi-empirical relationship<sup>55</sup> based on the radial crack generation during Vicker indentation when Young's modulus for ceramics is known (taken as 390 GPa for bulk  $\text{Al}_2\text{O}_3$ ).<sup>56</sup> Theoretical fracture toughness of the monolithic  $\text{Al}_2\text{O}_3$  is around  $3.3 \text{ MPa m}^{1/2}$  (Ref. [21]), but the highest value of fracture toughness for plasma sprayed  $\text{Al}_2\text{O}_3$  is  $\sim 2.0 \text{ MPa m}^{1/2}$  (Ref. [57]). In the current work, fracture toughness of the plasma sprayed  $\text{Al}_2\text{O}_3$  coating (A-SD) without CNT reinforcement was obtained as  $3.22 \pm 0.22 \text{ MPa m}^{1/2}$ , whereas plasma sprayed AC-B and AC-SD coatings displayed fracture toughness of  $3.86 \pm 0.16 \text{ MPa m}^{1/2}$  and  $4.60 \pm 0.27 \text{ MPa m}^{1/2}$  an improvement of 19.9 percent and 42.9 percent respectively, Figure 10. Student t-test was performed to confirm significant statistical difference between the mean fracture toughness values with more than 95% confidence level. Superior fracture toughness of AC-B and AC-SD nanocomposite coating is attributed to the retention and distribution of CNT as a reinforcing agent and synthesis of bimodal grain matrix. Fracture toughness improvement in AC-SD coating in comparison to AC-B coating is due to improved dispersion of CNTs in the matrix. CNT-bridging and CNT mesh formation provide additional toughening to the AC-SD coating.<sup>17, 24, 58</sup> Moreover, reduced thermal exposure to CNTs in AC-SD coating enhances partially melted region in the AC-SD coating, leading to improved energy absorption upon impact.

TEM analysis further corroborated the disparity of CNT dispersion in the  $\text{Al}_2\text{O}_3$  matrix. Figure 11(a) substantiated presence of comparatively large  $\text{Al}_2\text{O}_3$  grains and agglomerated CNTs in AC-B coating. This is expected

from the AC-B powder where CNTs are not uniformly dispersed as in case of AC-SD powder. Figure 11(b) shows TEM micrograph of AC-SD coating where a single CNT is visibly anchored in the molten region. Direct effect of anchoring via dispersed CNT in the molten region provides increased shock absorption and crack propagation resistance in AC-SD coating. Hence spray-drying treatment of AC-SD powder substantiates increase of fracture toughness via CNT dispersion effect. SAD pattern (inset in Figs. 11(a) and (b)) evinced presence of  $\alpha\text{-Al}_2\text{O}_3$  and  $\gamma\text{-Al}_2\text{O}_3$  in the coating, which is typical of plasma sprayed aluminum oxide.

Vicker indentation often generates crack in the ceramic structures because of stress relaxation upon unloading.<sup>59</sup> As observed in Figure 12(a), indentation crack is restrained by CNT bridges, Figure 12(b), across the propagating crack in AC-SD coating. Bridge structure reinforces the splat separation during crack propagation leading to topsy-turvy crack path. Hence, higher energy absorption regulates the reduced crack length to reinforce the integrity of the structure. Herein role of dispersed CNTs in AC-SD coating (Fig. 11(b)) provides multiple sites of anchoring and bridging the splats (Fig. 12(b)). In addition, solid-state sintered region fulfils the objective of terminating the propagating crack by providing the necessary sink for energy relaxation. Hence, optimized combination of powder treatment to uniformly distribute CNTs, and controlling the plasma parameters to obtain bimodal microstructure can greatly influence improvement in the fracture toughness of the plasma sprayed nanocomposite coating.

#### 4. CONCLUSIONS

(1) Plasma spraying has been successfully utilized to fabricate  $\text{Al}_2\text{O}_3$ -4 wt% CNT blend (AC-B) and composite spray dried  $\text{Al}_2\text{O}_3$ -4 wt% CNT (AC-SD) nanocomposite coating. Retention and distribution of CNTs was achieved indicating the survival of CNTs in the harsh plasma spraying environment.

(2) Powder feedstock treatment and optimized plasma processing has resulted in generating “bimodal” matrix microstructure where CNTs are well distributed in both coatings.

(3) Dispersion of CNTs in nanocomposite coating is dependent on the powder feedstock treatment. Preferential alignment of CNTs, and chain-loop anchoring of CNTs occurred in coatings synthesized with blended powder whereas CNT bridge formation, anchoring of CNTs in Al<sub>2</sub>O<sub>3</sub> melt and CNT mesh formation is observed in coating synthesized with spray dried powder.

(4) Addition of 4 wt% CNT has shown 19.9% improvement in AC-B-coating and 42.9% in the AC-SD coating respectively via Vicker indentation fracture toughness estimation of the nanocomposite coating.

**Acknowledgments:** Authors acknowledge the research funding from the Office of Naval Research (N00014-05-1-0398) to perform this work. Kantesh Balani and Tapas Laha acknowledge FIU Dissertation Year Fellowship whereas S. R. Bakshi acknowledges Presidential Enhanced Assistantship from Florida International University (FIU). Authors also acknowledge the assistance provided by Dr. Y. Liu, AMERI (Advanced Materials Engineering Research Institute), at FIU for facilitating SEM and TEM characterization.

## References and Notes

1. Y. Wang, S. Jiang, M. Wang, S. Wang, T. D. Xiao, and P. R. Strutt, *Wear* 237, 176 (2000).
2. G. R. Karagedov and N. Z. Lyakhov, *NanoStruct. Mater.* 11, 559 (1999).
3. H. Z. Wang, L. Gao, L. H. Gui, and J. K. Guo, *NanoStruct. Mater.* 10, 947 (1998).
4. W. Q. Li and L. Gao, *NanoStruct. Mater.* 11, 1073 (1999).
5. W. Nakao, M. Ono, S. K. Lee, K. Takahashi, and K. Ando, *J. Euro. Ceram. Soc.* 25, 3649 (2005).
6. R. Z. Ma, J. Wu, B. Q. Wei, J. Liang, and D. H. Wu, *J. Mater. Sci.* 33, 5243 (1998).
7. A. Peigney, E. Flahaut, C. Laurent, F. Chastel, and A. Rousset, *Chem. Phys. Lett.* 352, 20 (2002).
8. G. L. Hwang and K. C. Hwang, *J. Mater. Chem.* 11, 1722 (2001).
9. Y. Chen, C. Gan, T. Zhang, G. Yu, P. Bai, and A. Kaplan, *Appl. Phys. Lett.* 86, 251905 (2005).
10. P. Bansal, N. P. Padture, and A. Vasiliev, *Acta Mater.* 51, 2959 (2003).
11. C. Balazsi, F. Weber, Z. Kover, Z. Shen, Z. Konya, Z. Kasztovszky, Z. Vertesy, L. P. Biro, I. Kiricsi, and P. Arato, *Current Appl. Phys.* 6, 124 (2006).
12. G. D. Zhan, J. D. Kuntz, J. Wan, and A. K. Mukherjee, *Nat. Mater.* 2, 38 (2003).
13. X. Wang, N. P. Padture, and H. Tanaka, *Nat. Mater.* 3, 539 (2004).
14. K. Balani, R. Anderson, T. Laha, M. Andara, J. Tercero, E. Crumpler, and A. Agarwal, *Biomaterials* 28, 618 (2007).
15. J. Sun, L. Gao, and X. Jin, *Ceram. Intl.* 31, 893 (2005).
16. R. G. Duan, G. D. Zhan, J. D. Kuntz, B. H. Kear, and A. K. Mukherjee, *Scripta Mater.* 51, 1135 (2004).
17. G. D. Zhan, J. Kuntz, J. Wan, J. Garay, and A. K. Mukherjee, *J. Am. Ceram. Soc.* 86, 200 (2003).
18. G. D. Zhan, J. Kuntz, J. Wang, J. Garay, and A. K. Mukherjee, *Scripta Mater.* 47, 737 (2002).
19. G. D. Zhan, J. D. Kuntz, J. E. Garay, and A. K. Mukherjee, *Appl. Phys. Lett.* 83, 1228 (2003).
20. G. D. Zhan, J. D. Kuntz, H. Wang, C. M. Wang, and A. K. Mukherjee, *Phil. Mag. Lett.* 84, 419 (2004).
21. G. D. Zhan and A. K. Mukherjee, *Appl. Ceram. Tech.* 1 (2004).
22. G. D. Zhan, J. D. Kuntz, J. Wan, and A. K. Mukherjee, *Nature Mater.* 2, 38 (2003).
23. W. A. Curtin and B. W. Sheldon, *Mater. Today* 44, 44 (2004).
24. Z. Xia, L. Riester, W. A. Curtin, H. Li, B. W. Sheldon, J. Liang, B. Chang, and J. M. Xu, *Acta Mater.* 52, 931 (2004).
25. L. Chen, H. Ye, and Y. Gogotsi, *J. Am. Ceram. Soc.* 87, 147 (2004).
26. J. P. Fan, D. M. Zhuang, D. Q. Zhao, G. Zhang, M. S. Wu, F. Wei, and Z. J. Fan, *Appl. Phys. Lett.* 89, 121910 (2006).
27. M. Francke, H. Hermann, R. Wenzel, G. Seifert, and K. Wetzig, *Carbon* 43, 1204 (2005).
28. K. Hernadi, E. Ljubovic, J. W. Seo, and L. Forro, *Acta Mater.* 51 (2003).
29. G. Y. Li, P. M. Wang, and X. Zhao, *Carbon* 43 (2005).
30. J. Ning, J. Zhang, Y. Pan, and J. Guo, *Ceram. Intl.* 30, 63 (2004).
31. Y. S. Song and J. R. Youn, *Carbon* 43, 1378 (2005).
32. J. Sun and L. Gao, *Carbon* 41, 1063 (2003).
33. F. Becher, C. H. Hsueh, P. Angelini, and T. N. Tieg, *Theoretical and Experimental Analysis of the Toughening Behavior of Whisker Reinforcement in Ceramic Matrix Composites*, edited by S. Suresh and A. Needleman, Pergamon, New York (1989).
34. C. K. Chen, *ECERS* 25, 3293 (2005).
35. S. Maensiri, P. Laokul, L. Klinkaewnarong, and V. Amornkitbamrung, *Mater. Sci. Eng. A* 447, 44 (2007).
36. R. W. Siegel, S. K. Chang, B. J. Ash, J. Stone, P. M. Ajayan, R. W. Doremus, and L. S. Schadler, *Scripta Materialia* 44, 2061 (2001).
37. L. Xu, Z. Xie, L. Gao, X. Wang, F. Lian, T. Liu, and W. Li, *Ceramics International* 31, 953 (2005).
38. T. Laha, A. Agarwal, T. McKechnie, and S. Seal, *Mater. Sci. Eng. A* 381, 249 (2004).
39. T. Laha, S. Kuchibhatla, S. Seal, W. Li, and A. Agarwal, *Acta Mater.* 55, 1059 (2007).
40. T. Laha, A. Agarwal, and T. McKechnie, *The Minerals Metals and Materials Society, San Francisco, USA* (2005), p. 49.
41. S. O. Chwa, D. Klein, F. L. Toma, G. Bertrand, H. Liao, C. Coddet, and A. Ohmori, *Surf. Coat. Tech.* 194, 215 (2005).
42. E. T. Thostenson, Z. Ren, and T. W. Chou, *Comp. Sci. Tech.* 61, 1899 (2001).
43. J. Fan, D. Zhao, M. Wu, Z. Xu, and J. Song, *J. Am. Ceram. Soc.* 89, 750 (2006).
44. N. Ooi and J. B. Adams, *J. Comput. Electronics* 3, 51 (2004).
45. S. I. Cha, K. T. Kim, K. H. Lee, C. B. Mo, and S. H. Hong, *Scripta Mater.* 53, 793 (2005).
46. D. Goberman, Y. H. Soh, L. Shaw, E. Jordan, and M. Gell, *Acta Mater.* 50, 1141 (2002).
47. TAPP 2.2 ES Microwave Inc., in Hamilton, OH.
48. D. Srivastava, C. Wei, and K. Cho, *Appl. Mech. Rev.* 56, 215 (2003).
49. C. Q. Ru, *Phys. Rev. B* 62, 9973 (2000).
50. K. N. Ishihara, *Thermodynamics and Kinetics of Metastable Phase Formation* edited by C. Suryanarayana, Elsevier, Netherlands (1999), Vol 2, p. 5.
51. D. A. Porter and K. E. Easterling, *Phase Transformations in Metals and Alloys*, CRC Press (2001), p. 185.
52. K. Landry, S. Kalogeropoulou, and N. Eustathopoulos, *Mater. Sci. Eng. A* 254, 99 (1998).
53. O. H. Pakarinen, A. S. Foster, M. Paajanen, T. Kalinainen, J. Katainen, I. Makkonen, J. Lahtinen, and R. M. Nieminen, *Modeling and Simulation in Mater. Sci. Engg.* 13, 1175 (2005).

54. X. Tian and B. Bhushan, *J. Phy. D: Appl. Phy.* 29, 167 (1996).
55. G. R. Anstis, P. Chantikul, B. R. Lawn, and D. B. Marshall, *J. Am. Cer. Soc.* 64, 533 (1981).
56. J. Gong, Z. Peng, and H. Miao, *J. Europ. Ceram. Soc.* 25, 649–654 (2005).
57. V. Fervel, B. Normand, and C. Coddet, *Wear* 230, 70 (1999).
58. A. Peigney, C. Laurent, E. Flahaut, and A. Rousset, *Ceram. Intl.* 26, 677 (2000).
59. K. Balani, G. Gonzalez, A. Agarwal, R. Hickman, J. S. O'Dell, and S. Seal, *J. Am. Ceram. Soc.* 86, 1419 (2006).

Received: 14 February 2007. Revised/Accepted: 19 March 2007.